An improved OMI ozone profile research product version 2.0 with collection 4 L1b data and algorithm updates

Juseon Bak[1,*], Xiong Liu[2], Yang Kai[3], Gonzalo Gonzalez Abad[2],

Ewan O`Sullivan[2], Kelly Chance[2], Cheol-Hee Kim[1,4]

[1]Institute of Environmental Studies, Pusan National University, Busan 46241, Republic of Korea
[2]Smithsonian Astrophysical Observatory (SAO), Center for Astrophysics | Harvard & Smithsonian, Cambridge, MA 02138, USA
[3]Department of Atmospheric Sciences, University of Maryland, College Park, MD 20742, USA.
[4]Department of Atmospheric Sciences, Pusan National University, Busan 46241, South Korea

*Corresponding Author Juseon Bak (juseonbak@pusan.ac.kr) & Xiong Liu (xliu@cfa.harvard.edu)

Abstract

We describe the new and improved version (V2) of the ozone profile research product from the Ozone Monitoring Instrument (OMI) on the Aura satellite. One of the major changes is to switch the OMI L1b data from collection 3 to the recent collection 4 as well as the accompanying auxiliary datasets. The algorithm details are updated on radiative transfer (RT) model calculation and measurement calibrations, along with the input changes of meteorological data, and with the use of a tropopause-based ozone profile climatology, an improved high-resolution solar reference spectrum, and a recent ozone absorption cross-section dataset. A super Gaussian is applied to better represent OMI slit functions, instead of a normal Gaussian. The effect of slit function errors on the spectral residuals is further accounted for as pseudo absorbers in the iterative fit process. The OMI irradiances are averaged into monthly composites to reduce noise uncertainties in OMI daily measurements and to cancel out the common degradation of radiance and irradiance measurements which was previously neglected due to use of climatological composites. The empirical soft calibration spectra are re-derived to be consistent with the updated implementations and derived annually to remove the time-dependent systematic biases between measured and simulated radiances. The "common mode" correction spectra are derived from remaining residual spectra after soft calibration as a function of solar zenith angle. The common mode is included as a pseudo absorber in the iterative fit process, which helps to reduce the discrepancies of ozone retrieval accuracy between lower and higher solar zenith angles and between nadir and off-nadir pixels. Validation with ozonesonde measurements demonstrates the improvements of ozone profile retrievals in the troposphere, especially around the tropopause. The retrieval quality of tropospheric column ozone is improved with respect to the seasonal consistency between winter and summer as well as the long-term consistency before and after the row-anomaly occurrence.

38 **1. Introduction**
39

40   The Smithsonian Astrophysical Observatory (SAO) ozone profile algorithm was originally
41 developed to retrieve ozone profiles with sensitivity down to the lower troposphere from Global Ozone
42 Monitoring Experiment (GOME) measurements (Liu et al., 2005) and has been continuously adapted
43 to Ozone Monitoring Instrument (OMI) (Liu et al., 2010), GOME/2A (Cai et al., 2012), Ozone Mapping
44 and Profiler Suite (OMPS) (Bak et al., 2017), TROPOspheric Monitoring Instrument (TROPOMI)
45 (Zhao et al., 2021), Geostationary Environment Monitoring Spectrometer (GEMS) (Bak et al., 2019a),
46 and Tropospheric Emissions: Monitoring of Pollution (TEMPO) (Zoogman et al., 2017). The SAO
47 algorithm has been put into production in the NASA's OMI Science Investigator-led Processing System
48 (SIPS) to create the OMI ozone profile research product titled OMPROFOZ v0.93 that is publically
49 distributed via the Aura Validation Data Center (AVDC)
50 (https://avdc.gsfc.nasa.gov/pub/data/satellite/Aura/OMI/V03/L2/OMPROFOZ/). The OMPROFOZ
51 product has been contributed to a better understanding of chemical and dynamical ozone variability
52 associated with anthropogenic pollution over central and eastern China (Hayashida et al., 2015; Wei et
53 al., 2022), transport of anthropogenic pollution in free troposphere (Walker et al., 2010) and
54 stratospheric ozone intrusion (Kuang et al., 2017) as well as ozone concentration changes in the Asian
55 summer monsoon (Lu et al., 2018; Luo et al., 2018). Furthermore, this product has been used to quantify
56 the global tropospheric budget of ozone and evaluate how well current chemistry-climate models
57 reproduce the observations (Hu et al., 2017; Zhang et al., 2010). Compared to other similar space-borne
58 UV instruments, OMI has maintained much better long-term stability over the mission with low optical
59 degradation (1-2 % in radiance, 3-8 % in irradiance) and high wavelength stability (0.005-0.020 nm),
60 but there has been concern over the row anomaly effects appearing in 2007, becoming serious in early
61 2009, and currently damaging about half of the instrument's viewing capability (Schenkeveld et al.,
62 2017). So far, satellite ozone profile products have not been reliable for long-term analysis, especially
63 for the tropospheric ozone measurements due to their susceptibility to the optical degradation of
64 instruments (Gaudel et al., 2018). Ten-years of the OMPROFOZ product were assessed in-depth in
65 Huang et al. (2018;2017) through the spatiotemporal validation using global reference dataset collected
66 from in-situ ozonesonde and space-borne Microwave Limb Sounder (MLS) measurements. They
67 concluded noticeable discrepancies in time-series of data quality due to the occurrence of serious row
68 anomaly and the dependence of retrieval quality on the latitude/season/viewing geometries. Since the
69 first release of OMPROFOZ data, implementation details have been externally refined to improve the
70 retrieval quality. Bak et al., (2013) demonstrated improvements of ozone profile retrievals around the
71 extratropical tropopause area by better constraining climatological a priori information. To better

Atmospheric
Measurement
Techniques
Discussions

72   represent an instrument spectral response function (ISRF), Sun et al. (2017) employed a Super Gaussian

73   function which can represent more complex shapes compared to a classical Gaussian function. The slit

74   function linearization was experimented in Bak et al. (2019b) to account for the effects of errors in slit

75   function parameters on the spectral fit residuals. Moreover, the best spectroscopic inputs were

76   investigated with respect to the ozone cross-section (Bak et al., 2020; Liu et al., 2013) and the high-

77   resolution solar reference spectrum (Bak et al., 2022). To accelerate the time-consuming radiative

78   transfer calculation, a principal component analysis (PCA)-based radiative transfer (RT) model was

79   employed as a forward model with the correction scheme of RT approximation errors using look-up

80   tables (LUTs) (Bak et al., 2021). The updates to radiometric corrections were made with the time-

81   dependent soft calibration and solar zenith angle dependent common mode correction, improving the

82   spatiotemporal consistency of retrieval quality, which are detailed in this paper. Individual refinements

83   mentioned above are incorporated in the OMPROFOZ V2 algorithm, along with the switch of OMI L1b

84   data product from collection 3 to collection 4. Note that OMI measurements have been reprocessed to

85   deliver the new collection 4 dataset which supersedes and improves the collection 3 with respect to the

86   ongoing instrument effects and optical degradations, drifts in electronic gain, and pixel quality flagging.

87   (Kleipool et al., 2022).

88   In this paper we describe updates made in the OMI ozone profile algorithm, discuss their impact on

89   spectral fit and ozone profile retrievals, and provide an initial quantitative assessment of tropospheric

90   ozone columns with respect to their long-term consistency. Section 2 describes OMI L1b and auxiliary

91   products used in retrieving ozone profiles, along with the retrieval methodology and OMPROFOZ v2

92   product. In section 3 the updates of implementation details are specified and verified. Section 4 presents

93   the validation results using ozonesonde measurements. This paper is summarized and concluded in

94   Section 5.

2. Description of the SAO OMI ozone profile algorithm and OMPROFOZ product

2.1 OMI products

100   Table 1 lists the OMI standard or auxiliary products used in reprocessing OMI ozone profiles,

101   which are publicly available through NASA's Goddard Earth Sciences Data and Information Services

102   Center (GES DISC). OMI is a nadir-viewing UV and visible spectrometer in which two-dimensional

103   (spectral × spatial) charged-coupled device (CCD) detectors are employed. The collection 4 L0-1B

104   processor was newly built based on the TROPOMI L0-1B processor at the OMI SIPS, which produces

105   radiometrically calibrated and geolocated solar irradiances and earthshine radiances from the raw sensor

106   measurements. Insights learned from the usage of OMI collection 3 data over the past 17 years are

107   leveraged to correct optical and electronic aging and improve pixel quality flagging. The details of

108   updates and improvements from collection 3 to 4 can be found in Kleipool et al. (2022). The

109   OML1BIRR (10.5067/Aura/OMI/DATA1401) provides the daily averaged irradiance measurements.

110   The OML1BRUG (10.5067/AURA/OMI/DATA1402) contains Earth view spectral radiances taken in

111   the global mode from the UV detector. To increase a signal to noise ratio (SNR) at shorter UV

112   wavelengths, a measured spectrum is divided into two sub channels at ~ 310 nm and then the spatial

113   resolution of the shorter spectra is degraded by a factor of 2 in cross-track pixels, resulting into 48 km

114   and 24 km at nadir for 159 channels in the Band 1 (UV-1, 264-311 nm) and for 557 channels in the

115   Band 2 (UV-2, 307-383 nm), respectively. The spatial resolution is 13 km in the flight direction. Cloud

116   information is taken from OMCLDO2 based on the spectral fitting of O_2-O_2 absorption band at 477 nm,

117   while a climatological surface albedo is taken from OMLER. The OMUANC is a new ancillary product

118   geo-collocated to UV2 spatial pixels, developed for supporting the production of the OMI L2 data

119   products. We use OMUANC data for taking snow ice flags and row anomaly flags. The row anomaly

120   is an anomaly which affects the quality of the level 1B radiance data at all wavelengths for specific

121   viewing angles. Only two of OMI's 60 rows were initially affected in 2007, but the anomalies have

122   become more serious since January 2009 (~ 30%), spreading to ~ 50 % (rows 25-55) during the period

123   of 2010-2012. There is no reliable correction scheme for the row anomaly-affected measurements and

124   therefore flagging the row anomalies as bad data is important to assure the L2 product quality. Row

125   anomaly flags are available from both OML1BRUG and OMUANC; the former is based on analysis of

126   features observed in the radiance measurements to identify the row anomaly contained pixels, referred

127   as to the KNMI flag. Note that the KNMI flagging method remains unchanged from collection 3 to 4

128   (AURA-OMI-KNMI-L01B-0005-SD, 2021). The NASA flag for the latter is based on a statistical

129   analysis of errors detected in the NASA OMTO3 L2 total column ozone. According to Schenkeveld et

130   al. (2017) who compared the KNMI and NASA flagging results in the UV2 channel, two methods

131   produce consistent flagging results over the full course of the OMI mission, but the NASA method is

132   likely to be stricter and reliable. In this paper, row anomalies are filtered out when either OML1BRUG

133   or OMUANC flags are flagged. The OMUFPMET and OMUFPSLV supply meteorological fields at

134   OMI overpass positions, which is further detailed in Section 3.2 where the updates to meteorological

135   inputs in OMPROFOZ are verified. In addition, OMI total column ozone product (OMTO3G) is used

136   in deriving empirical correction spectra.

137

138 **Table 1 Input list of OMI data.**

Product name	Processing level (spatial resolution/band [*])	Collection number	Primary variables
OML1BIRR	L1B (UV1,UV2)	4	solar irradiance
OML1BRUG	L1B (UV1, UV2)	4	Earthshine radiance
OMCLDO2	L2 (UV2)	3	cloud fraction, cloud pressure
OMUANC	L2 (UV2)	4	Row anomaly flag, snow ice flag
OMUFPMET	L2 (UV2)	4	Pressure profile, temperature profile
OMUFPSLV	L2 (UV2)	4	Surface pressure, surface skin temperature, Thermal tropopause pressure
OMLER	L3 (0.5° x 0.5°)	3	Monthly and yearly climatology of the Earth's surface Lambert Equivalent Reflectance (LER)
OMTO3G	L3 (0.25° x 0.25°)	3	Total column ozone

139 [*] UV1, UV2, VIS represent bands and their corresponding spatial resolutions (except for OML1BIRR) 13 x 48

140 km^2, 13 x 24 km^2, and 13 x 24 km^2 at nadir, respectively.

141

142

2.1 OMPROFOZ algorithm

144

145   In our algorithm, two spectral windows are selected for 270-309 nm in the UV-1 band and 312-

146 330 nm in the UV-2 band and two UV-2 spatial pixels are co-added to match UV-1 spatial resolution.

147 To meet the computational budget in the previous data processing, OMI measurements were spatially

148 coadded in the flight direction, reducing the spatial resolution to 48×52 km^2 in the v1 product. In the

149 v2 data processing, PROFOZ will be released at 38×26 km^2, owing to the speed up of radiative transfer

150 calculations described in Section 3.7. The SAO ozone profile algorithm is composed of an optimal

151 estimation (OE) based inversion (Rodgers, 2000), radiative transfer (forward) model simulations, and

152 state-of-the-art calibrations (Figure 1).

153   **In the calibration process**, a cross-correlation technique is implemented to characterize in-orbit

154 slit functions and wavelength shift errors using a well calibrated, high resolution solar reference

155 spectrum. OMI has shown high wavelength stability (0.005-0.020 nm) over the mission lifetime (Bak

156 et al., 2019b; Schenkeveld et al., 2017; Sun et al., 2017) and thereby additional wavelength correction

157 is not carried out for each radiance and irradiance spectrum. The empirical correction so-called soft

158 calibration is applied for eliminating the systematic measurement biases in the wavelength range of 270

159 - 330 nm for ozone fitting and around 347 nm for the initial surface albedo/cloud fitting. This correction

Atmospheric
Measurement
Techniques
Discussions
Open Access
EGU

160 was previously applied dependent on wavelength and cross-track position, but currently updated to

161 enable a correction for time-dependent degradation (Section 3.8).
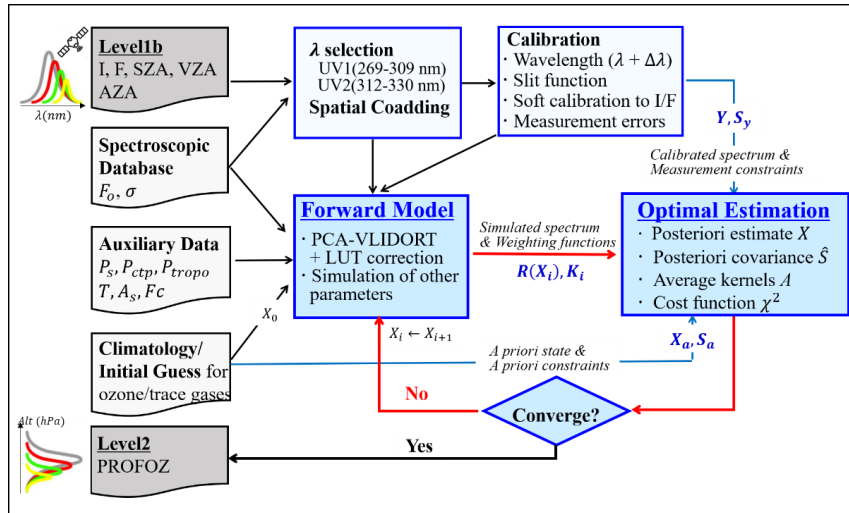
Figure 1. Flow chart for retrieving ozone profiles with optimal estimation-based inversion.

164

165 **This OE-based inversion** is physically regularized toward minimizing the difference between a

166 measured spectrum Y and a spectrum that is simulated by the forward model $\mathbf{R}(X)$, constrained by

167 measurement error covariance matrix $\mathbf{S_y}$ and statistically regularized by an a priori state vector X_a

168 and error covariance matrix $\mathbf{S_a}$. The solution at iteration step $i+1$ is written as

169
$$X_{i+1} = X_i + (\mathbf{K}_i^T \mathbf{S}_y^{-1} \mathbf{K}_i + \mathbf{S}_a^{-1})^{-1} [\mathbf{K}_i^T \mathbf{S}_y^{-1} (Y - \mathbf{R}(X_i)) - \mathbf{S}_a^{-1}(X_i - X_a)] \ , \tag{1}$$

170 where each component of $\mathbf{K}$ is the derivative of the forward model, called the Jacobians or weighting

171 function matrix. Y is composed of the logarithm of the sun-normalized radiance. To construct $\mathbf{S_y}$,

172 the normalized random-noise errors of radiance and irradiance taken from OMI L1b products are summed

173 up as total measurement errors. The measurement errors are typically underestimated and then noise

174 floors (0.4 % below 310 nm, 0.15-0.2% above) are imposed on as a minimum value. Note that $\mathbf{S_y}$ is a

175 diagonal matrix, assuming that measurement errors are uncorrelated among wavelengths.

176 The optimal estimate is iteratively updated until convergence when the relative change in the cost

177 function between previous and current iterations is less than 1.0 %. The cost function χ^2 is given by

178 $$\chi^2 = \left\|\mathbf{S}_y^{-\frac{1}{2}}\{\mathbf{K}_i(\boldsymbol{X}_{i+1} - \boldsymbol{X}_i) - [\boldsymbol{Y} - \mathbf{R}(\boldsymbol{X}_i)]\}\ )\right\|_2^2 + \left\|\mathbf{S}_a^{-\frac{1}{2}}(\boldsymbol{X}_{i+1} - \boldsymbol{X}_a)\ \right\|_2^2. \tag{2}$$

179 Maximum number of iterations is set to be 10 against the divergence. Typically, it takes 2-3 iterations

180 to converge, but increasing to 6-7 for thick clouds.

181   **The state vectors** to be fitted in OMPROFOZ v2 are listed in Table 2, together with their a priori

182 value and a priori error. Compared to OMPROFOZ v1, three kinds of parameters are newly added to

183 implement the slit function linearization and common mode correction as a pseudo absorber. A *priori*

184 value and error are set empirically for spectroscopic parameters, and are taken from climatological

185 datasets for geophysical parameters such as atmospheric ozone and surface albedo. They are assumed

186 to be uncorrelated between fitting parameters, except for a priori ozone error covariance matrix with

187 the correlation length of 6 km. Cloud fraction is initially taken from OMCLDO2 and fitted at 347 nm

188 together with initial surface albedo taken from OMLER.

189 **Table 2**. List of fitting variables, a priori values and a priori errors. A correlation length of 6 km is used
190 to construct the a priori covariance matrix for ozone variables. All the other variables are assumed to be
191 uncorrelated with each other.
192

Fitting variales	# Variables	A priori	A priori error
Ozone at each layer	24	Climatology	Climatology
Surface albedo	2 (1 for each channel)	Climatology	0.05
First-order wavelength-dependent term for surface albedo	1 (only UV2)	0.0	0.01
Cloud fraction	1 (only UV2)	Derived from 347 nm	0.05
Radiance/irradiance wavelength shifts	2 (each channel)	0.0	0.02 nm
Radiance/O_3 cross section wavelength shifts	2 (each channel)	0.0	0.02 nm
Ring scaling parameters	2 (each channel)	-1.87	1
offset parameters in radiance	2 (each channel)	0.0	1.0^{-4}
Slit width coefficient	2 (each channel)	0.0	0.1 nm
Shape factor coefficient	2 (each channel)	0.0	0.1
Common mode scaling parameters	2 (each channel)	1.0	1.0

193
194
195
196
197

2.3 OMPROFOZ product

The previous version product was stored in the HDF-EOS5 format, but the NetCDF-4 format is applied to create the OMPROFOZ v2 product, similar to other collection 4 OMI data products. Also it is written using the TEMPO output libraries so that it shares common data structures and metadata definitions with TEMPO data products.

The main product parameters are partial ozone columns at 24 layers, ~ 2.5 km for each layer, from the surface to ~ 65 km in the unit of Dobson Unit (DU, 1 DU = 2.69x10^{16} molecules.cm^{-2}). The 25-level vertical pressure grid is set initially at $P_i = 2^{-i/2}$ atm for i=0, 23 and with the top of the atmosphere set for P_{24}. This pressure grid is then modified: the surface pressure and the thermal tropopause pressure are used to replace the level closest to each one, and tropospheric layers are distributed equally with logarithmic pressure. Correspondingly, the random-noise error and solution error profiles are provided in terms of a square root of diagonal elements of random-noise error covariance matrix $\mathbf{S_n}$ and solution error covariance matrix $\mathbf{\hat{S}}$ that is directly estimated from the retrievals:

$$\mathbf{S_n} = \mathbf{G S_y G^T}, \ \mathbf{\hat{S}} = \left(\mathbf{K^T S_y^{-1} K} + \mathbf{S_a^{-1}}\right)^{-1}, \text{ and } \mathbf{G} = \mathbf{\hat{S} K^T S_y^{-1}}, \tag{3}$$

where $\mathbf{G}$ is the matrix of contribution functions. The smoothing error covariance $\mathbf{S_s}$ can be also directly estimated, but is not provided in the output file. That is because it can be derived with the following relationship:

$$\mathbf{\hat{S}} = \mathbf{S_s} + \mathbf{S_n}. \tag{4}$$

$$\mathbf{S_s} = (\mathbf{A} - \mathbf{I})\mathbf{S_a}(\mathbf{A} - \mathbf{I})^{\mathrm{T}}, \tag{5}$$

where $\mathbf{I}$ is the unit vector and $\mathbf{A}$ is the matrix of averaging kernels:

$$\mathbf{A} = \frac{\partial X}{\partial X_T} = \left(\mathbf{K^T S_y^{-1} K} + \mathbf{S_a^{-1}}\right)^{-1} \mathbf{K^T S_y^{-1} K} = \mathbf{\hat{S} K^T S_y^{-1} K} = \mathbf{GK}. \tag{6}$$

A particular row of $\mathbf{A}$ describes how the retrieved profile in a particular layer is affected by changes in the true profile in all layers. It is a very useful variable to characterize the retrieval sensitivity and vertical resolution of the retrieved profile. The diagonal elements of A, known as Degrees of Freedom for Signal (DFS) represent the number of useful independent pieces of information available at each

Atmospheric
Measurement
Techniques
Discussions

231 layer from the measurement. To quantify the performance of the spectral fitting, the mean fitting

232 residuals are calculated for each fitting window (UV1, UV2), in the form of the root mean square of

233 spectral differences relative to the measured spectrum and the measured error as follows:

234

235 $$\text{RMS} = \sqrt{\frac{1}{N}\sum_1^N((I_m - I_s)/I_m)^2} \times 100 \ (\%), \quad \text{and RMSE} = \sqrt{\frac{1}{N}\sum_1^N((I_m - I_s)/I_e)^2}. \ (7)$$

236

237 where I_m, I_s, and I_e represent measured spectrum, simulated spectrum, and measured errors,

238 respectively, with N the number of the wavelengths in each window. The RMS of fitting residuals

239 needs to be better than 0.2-0.3 % in the Huggins band (310-340 nm) for reliable retrievals of

240 tropospheric ozone (Munro et al., 1998). The RMSE describes both spectral fit quality and the stability

241 of regularization. The ideal value of RMSE is one. If RMSE $\ll 1$, either the fitting is overfitted or the

242 measurement errors are overestimated. On the other hand, if RMSE $\gg 1$, either the fitting is

243 underfitted or the measurement errors are underestimated.

244

245 **3. Specification and verification of updated implementations**

246

247 This section specifies new and improved updates made in the OMPROFOZ algorithm, listed in

248 Table 3. The corresponding impacts on the spectral fit and ozone retrievals are verified. Note that the

249 verification results of several implementations have already been presented in companion papers

250 indicated in the fourth column of Table 3, which is briefly described in this paper. The unpublished

251 implementations are specifically described in this paper.

252

253 **Table 3.** Lists of updates on algorithm implementations

Implementations	OMPROFOZ v1	OMPROFOZ v2	Verification
A priori ozone climatology	Latitude dependent monthly profiles	Latitude and tropopause (daily) dependent monthly profiles	Bak et al. (2013)
Meteorological data	NCEP	OMUFPSLV(Joiner, 2023a) OMUFPMET(Joiner, 2023b)	This work
Irradiance	Climatological composite	Monthly composite	This work
Solar reference spectrum	Chance and Kurucz (2010)	Coddington et al. (2021)	Bak et al. (2022)
Slit function	Gaussian parameterization	Super Gaussian parameterization and linearization	Bak et al. (2019b)
Ozone cross section	BDM (Brion et al., 1993; Daumont et al., 1992; Malicet et al., 1995)	BW (Birk and Wagner, 2018)	Bak et al. (2020)
Radiative transfer calculation	VLIDORT only	PCA-VLIDORT	Bak et al. (2021)
Radiometric	CCD dependent soft calibration	- CCD and time	This work

calibration		dependent soft calibration - Common mode correction	

254

## 3 .1 A priori ozone climatology

256   An optimal estimation-based ozone retrieval can be significantly affected by the quality of a priori

257 data given insufficient measurement information. Therefore, the constraint can push the retrieval away

258 from the actual state of the atmosphere towards a priori information, especially near the boundary layer

259 or the tropopause where the vertical resolution of nadir satellite observations is inherently limited. In

260 the v1 algorithm, the a priori ozone information was taken from McPeters et al. (2007) (abbreviated as

261 LLM climatology) consisting of monthly average ozone profiles for every 10°-latitude zone based on

262 ozonesonde measurements in the troposphere and lower stratosphere and satellite measurements above.

263 The v2 algorithm implements a tropopause-based (TB) ozone profile climatology from which a zonal

264 monthly mean profile is vertically adjusted according to the tropopause height taken from the daily

265 meteorological database described in Sect. 3.2. Applying the TB climatology as OMI a priori was

266 thoroughly verified in Bak et al. (2013) who demonstrated improvements of OMI ozone profile

267 retrievals in comparison with ozonesondes as well as in representing the sharp gradients of ozone

268 vertical structures near the tropopause. Figure 2 compares tropospheric ozone retrievals on 01 February

269 2007 with a priori ozone constraints being taken from LLM and TB, respectively. The most noticeable

270 difference is identified in the northern region of Europe where abnormally high concentrations are

271 retrieved when LLM is used as a priori. This retrieval issue was also mentioned in comparing

272 OMPROFOZ v1.0 with other satellite products, data assimilation, and chemical transport model

273 calculation (Gaudel et al., 2018; Ziemke et al., 2014), showing large positive biases in tropospheric

274 column ozone during high-latitude winter, but it has not been explained. It is clearly seen that the

275 abnormal feature of the retrieved high ozone is closely correlated with the high LLM a priori (Fig. 2.c)

276 resulting from abnormally low tropopause pressure or high tropopause height (Fig. 2.e). LLM can

277 represent the typical vertical profiles whose ozonepause is located at ~ 8 km over high latitudes during

278 the winter. Therefore, with the presence of the abnormally high tropopause height, the lower

279 stratospheric layers of LLM profiles can be misrepresented as a priori in the upper tropospheric ozone

280 layers, which likely causes the large positive biases of ozone retrievals in the troposphere seen in

281 OMPROFOZ v1. However, an ozone profile taken from the TB climatology is re-distributed according

282 to the daily tropopause which becomes an ozonepause of TB profiles. In the subtropical region, LLM

283 may also provide incorrect information in the presence of high tropopause height, but ozone retrievals

284 are less affected, implying that OMI retrievals are less constrained by the a priori information in this

Atmospheric
Measurement
Techniques

Open Access

EGU

Discussions

285   case due to more measurement information, unlike in the northern high-latitudes.

286

287

288
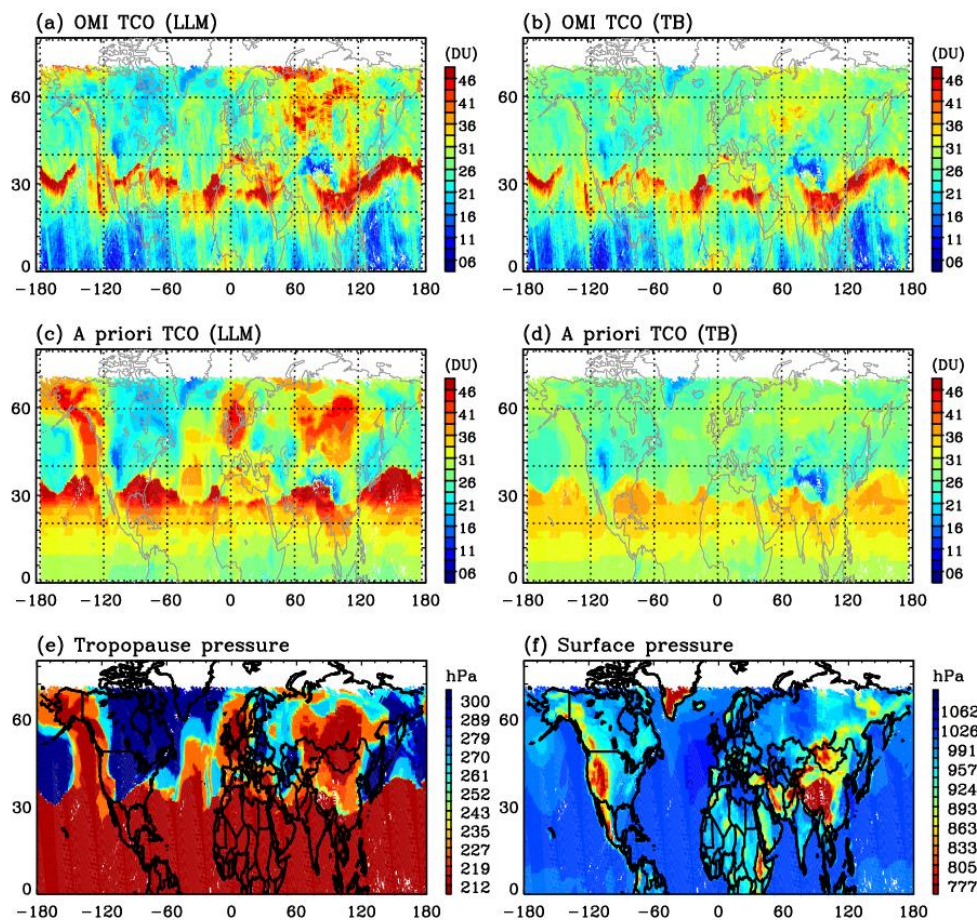
Figure 2. Comparison of (a,b) OMI tropospheric column ozone (TCO) and (c,d) the corresponding a priori TCO
taken from monthly and zonal mean climatologies (LLM/left, TB/right), respectively, in the Northern hemisphere
on 01 February 2007. (e) tropopause and (f) surface pressure fields are presented in the bottom panels.

292

293   **3.2 Meteorological data**

294   As a forward model input, the surface pressure is required to define the bottom of the atmosphere,

Atmospheric
Measurement
Techniques
Discussions

295   with the air temperature profile to account for the temperature dependence of the ozone absorption cross

296   section, especially in the Huggins band. The tropopause pressure is also required to be used as one of

297   the retrieval vertical levels to separate stratospheric ozone from tropospheric ozone, and determine the

298   a priori ozone profile in the case of using the TB climatology in v2. These meteorological variables

299   were taken externally from National Centers for Environmental Prediction (NCEP) reanalysis data

300   (http://www.cdc.noaa.gov), which provide 6-hourly (4 time a day) global analyses at 2.5 ° x 2 ° grids

301   with 17 vertical pressure levels below 10 hPa. These databases were pre-interpolated to 1:45 PM local

302   solar time when OMI is crossing at equator and OMI's ground pixels using nearest neighbor

303   interpolation and then manually transmitted to OMI SIPS. However, the data transmission has been

304   accidently halted since June 2011 and hence climatological monthly mean data have been used as a

305   back-up in the data processing. To avoid this risk, the meteorological input is switched to the internal

306   meteorological products, geo-collocated to OMI UV-2 1-Orbit L2 Swath from the 2D Time-Averaged

307   Single-Level Diagnostics (OMUFPSLV) (Joiner, 2023a) and the GEOS-5 FP-IT 3D Time-Averaged

308   Model-layer Assimilated data (OMUFPMET) (Joiner, 2023b). We take the average air temperature

309   given at 72 pressure levels above the center of the ground pixel from OMUFPMET as well as surface

310   temperature, surface pressure, and thermal tropopause pressure at the center of the ground pixel from

311   OMUFPSLV. The impact of switching meteorological input on the spectral fitting residuals is

312   insignificant (not shown here), implying that the residuals might be absorbed by other state vectors.

313   Figure 3 illustrates that ozone profile retrievals are changed by 2-3 DU, especially in the tropopause

314   region due to changes of a priori ozone profiles in adjusting the climatological TB ozone profile around

315   the daily tropopause height.
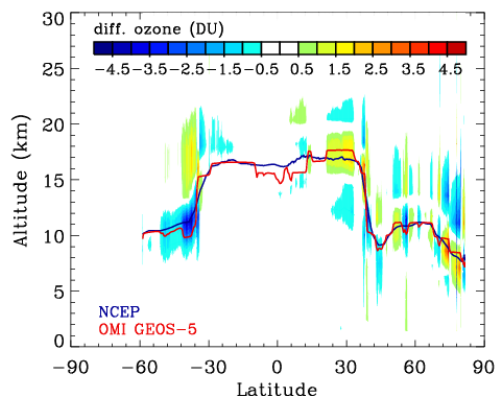
316

317   **Figure 3.** Differences of OMI ozone profile retrievals (DU) along the nadir view from 7th orbit of measurements
318   on 15 Jun 2006, due to switching the meteorological input from NCEP to OMI GEOS-5 (OMUFPSLV and
319   OMUFPMET). The solid line represents the tropopause height from NCEP (blue) and OMI GEOS-5 (red).

Atmospheric
Measurement
Techniques
Discussions

3.3 Ozone cross section

The BDM cross-section measurements have been the standard input for retrieving ozone profiles using BUV measurements over the last decade (Liu et al., 2013, 2007; Orphal et al., 2016). In a companion paper (Bak et al., 2020), the new BW ozone cross-section dataset was tested to check if there is room to improve our ozone profile retrievals, which made us switch the cross section from BDM to BW in OMPROFOZ v2. As illustrated in Figure 4 (upper), the BW dataset provides improved temperature coverage from 193 K to 293 K, every 20 K over the BDM dataset given only at five temperatures above 218 K. Therefore, BW measurements were better parameterized as quadratic temperature-dependent coefficients with uncertainties of 0.25-2 % whereas for BDM measurements fitting residuals of 2-20 % remains. Note that parameterized coefficients of cross-section measurements are typically applied in both column ozone and ozone profile retrievals for conveniently representing the temperature dependence of cross-section spectrum. Bak et al. (2020) also demonstrated the improved performance of ozone profile retrievals through comparison with ozonesonde measurements, showing a significant reduction of the standard deviations, by up to 15 % in the lower stratosphere and upper troposphere where atmospheric temperatures are lower than ~ 200 K.
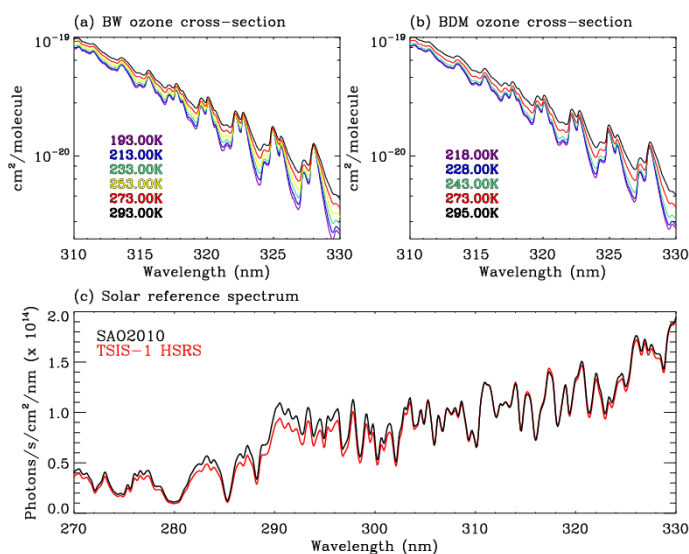
Figure 4. Comparisons of (a.b) ozone cross-sections and (c) solar reference spectrum used in OMPROFOZ v1 and v2 algorithms. Note that high-resolution solar reference spectrum is convolved with a Gaussian slit function of 0.4 nm FWHM (Full Width at Half Maximum) resolution.

Atmospheric
Measurement
Techniques
Open Access
EGU
Discussions

3.4 High-resolution solar reference spectrum

An accurate, high-resolution extraterrestrial solar reference spectrum is required for either wavelength calibration or slit function characterization. We decided to switch the solar reference spectrum from Chance and Kurucz, (2010) to Coddington et al., (2021). Figure 4.c illustrates radiometric discrepancies between the new solar reference called the TSIS-1 Hybrid Solar Reference Spectrum (HSRS) and the old solar reference called the SAO2010. A companion paper evaluated that the radiometric uncertainties of the new reference spectrum are below ~ 1 % whereas for SAO2010 those range from 5% in the longer UV part to 15 % in the shorter UV part (Bak et al., 2022). Furthermore, they confirmed an opportunity to improve the spectral fitting of slit functions and hence the spectral fitting of ozone when using the TSIS-1 spectrum; the impact on ozone profile retrievals is 5-7 % in the troposphere.

3.5 Solar irradiance spectrum

OMI makes solar irradiance measurements near the northern hemisphere terminator of an orbit once per day, which are required to calculate top-of-atmosphere reflectance and to estimate an on-orbit slit function in ozone profile retrievals. In order to reduce the short-term noise of OMI individual measurements, the v1.0 algorithm implemented the use of climatological solar spectra derived from three years of daily OMI Level 1B product (2005-2007). In the v2.0 algorithm, irradiance spectra are tabled as a monthly average to reduce the short-term noise as well as cancel out the common degradation existing in radiance and irradiance. Figures 5 and 6 compare irradiance measurements averaged over July for each year from collection 4 and collection 3, respectively. Collection 3 shows significant short-term noise in daily measurements in the UV2 range, around 3-5 % and also systematically decreasing patterns of monthly irradiance spectra from – 10 % in the UV1 range and -6 % in the UV2 range over the mission. Collection 4 provides much improved irradiance spectra with respect to both degradation and noise errors. In addition, OMI random-noise errors in the monthly average spectra are compared. Collection 4 ranges from 0.02 % in the UV1 and 0.04 % in the UV2, consistently over the mission. However, collection 3 shows somewhat different features in the UV2 range, like more wavelength dependence and a systematic drift as of 2008-2009. Figure 7 shows the impact of switching OMI level1b product from collection 3 to 4 on fitting residuals resulting from ozone profile retrievals on 16 July 2020; the average fitting residuals are plotted as a histogram for each fitting window. In this experiment the v2 implementations are identically applied without radiometric corrections (soft calibration and common mode correction are turned off). In addition, the impact of using monthly and daily irradiance is investigated. As shown, fitting residuals are noticeably improved in both fitting windows due to

373   switching from collection 3 to 4. This experiment illustrates that monthly irradiances should be used

374   instead of daily measurements when using the collection 3 product. In comparison, the corresponding

375   impact on fitting residuals with collection 4 product is not very significant due to improvements of

376   short-term noise errors in daily irradiance measurements, but the number of retrievals with smaller

377   fitting residuals increases in the UV2 band.
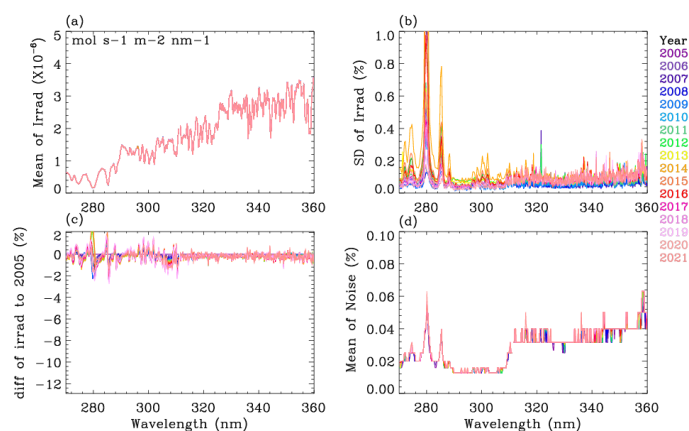
378

379   **Figure 5.** (a) Monthly mean irradiance spectra of OMI collection 4 product in July from 2005 to 2021 at the

380   10th cross-track position for UV-1 band and 20th cross-track position for UV-2 band without coadding. (b)

381   Corresponding standard deviations of the monthly mean irradiances, (c) Biases of the mean irradiances relative

382   to 2005, and (d) Monthly mean random noise errors.
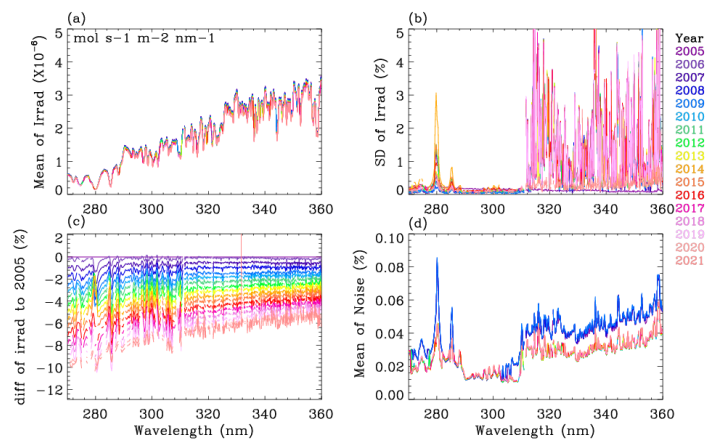
383

384   **Figure 6**. Same as Figure 5, but for OMI collection 3 irradiance product.

385
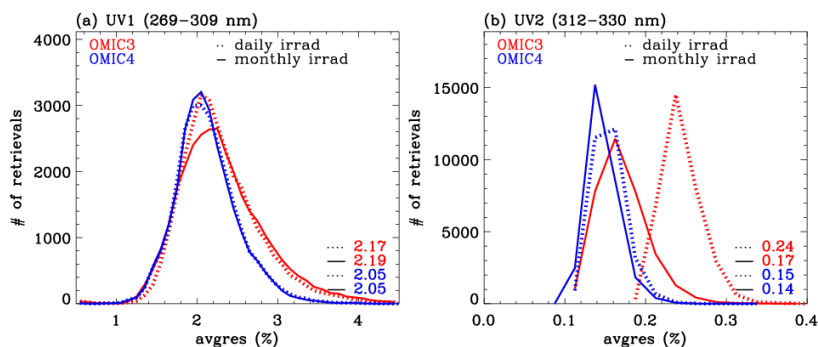
Figure 7. Histograms of average fitting residuals from OMI collection 3 (red) and 4 (blue) level 1b products on 15 July 2020, in (a) UV1 and (b) UV2 ranges, respectively. In order to make a fair comparison, this experiment limits OMI measurements to the western side of the swath to avoid using row anomaly cross-track pixels and empirical recalibration is not applied. Fitting residuals are evaluated with both daily (dashed) and monthly mean (solid) OMI irradiance measurements. The median values of average fitting residuals are presented in the legend.

3.6 Instrument spectral response function (ISRF) parameterization and linearization

OMI ISRFs were previously parameterized as a standard Gaussian by fitting the slit width (w) from OMI solar irradiances separately for each channel and each cross-track position. In the updated implementation, one more parameter, shape factor (k) is added to parameterize ISRFs as a Super Gaussian ($S(\Delta\lambda) = exp\left[-\left|\frac{\Delta\lambda}{w}\right|^{k}\right]$). However, slit functions in radiance could deviate from those derived from solar spectra due to the sensitivity to scene heterogeneity, differences in stray light between radiance and irradiance, and intra-orbit instrumental changes. These might cause some spectral structures in the radiance fitting. Therefore, the v2 algorithm treats these spectral errors as Pseudo Absorbers (PAs), which is derived as $\frac{\partial I}{\partial p} = \frac{\partial S}{\partial p} \otimes I_h$ (p = w or k) through the slit function linearization. As specified in Table 2, these PAs are iteratively adjusted with zero-order scaling parameter. The description and evaluation of this implementation for OMI ozone profile retrievals is detailed in a companion paper (Bak et al., 2019b).

3.7 Radiative Transfer Calculation

The radiative transfer (RT) model is needed for calculating the forward model component such as top-of-the-atmosphere radiances, and Jacobians of radiances with respect to the atmospheric and surface parameters. The radiance calculation is made for a Rayleigh atmosphere (no aerosols) with Lambertian

410   reflectance assumed for the surface and for clouds. The Independent Pixel Approximation (IPA) is

411   employed to treat partial clouds by assuming a cloud reflectivity of 80 %: $I = I\ (R_{sfc}, P_{sfc})(1 - f_c) +$

412   $I\ (R_{cloud}, P_{cloud})$. Individual radiances need to be simulated at finer grids than at least 4 pixels per

413   FWHM so that the spectral convolution is applied to account for OMI spectral resolution. To reduce the

414   computational burden, a few wavelengths are effectively selected (λ_e) for running RT model and then

415   interpolated to regular high-resolution grids (λ_h) with the radiance adjustment for errors caused by the

416   spectral resolutions as follows:

417   $$I(\lambda_h) = I(\lambda_e) + \sum_{l=1}^{N} \frac{\partial I\ (\lambda_e)}{\partial \Delta_l^{gas}} \left(\Delta_l^{gas}(\lambda_h) - \Delta_l^{gas}(\lambda_e) \right) + \frac{\partial I\ (\lambda_e)}{\partial \Delta_l^{ray}} \left(\Delta_l^{ray}(\lambda_h) - \Delta_l^{ray}(\lambda_e) \right), \qquad (7)$$

418   where $\frac{\partial I}{\partial \Delta_l}$ represents for Jacobians with respect to optical properties at layers l (l = 1 to N). In the v2

419   forward model, both λ_c and λ_h are set to be finer than intervals previously used as noted in Table 4

420   where the implementation details between v1 and v2 forward models are compared. To accelerate RT

421   calculations, the RT model is switched from VLIDORT v2.4 to PCA-based VLIDORT v2.8; multiple

422   scattering (MS) calculations are performed at individual wavelengths in the former whereas MS

423   calculations in the latter are performed only for a few EOF-derived optical states which are developed

424   from spectrally binned sets of inherent optical properties that possess some redundancy. In both v1 and

425   v2 forward models, the polarization is not part of the direct RT simulation of the entire spectrum, but a

426   polarization correction is applied to speed up the RT. In the v1 forward model, vector calculations are

427   additionally executed at 14 wavelengths to calculate the scalar vs. vector differences at these

428   wavelengths which are then interpolated to every wavelength. However, residual polarization errors

429   remain along with other approximation errors arising from using 4 half-streams and coarse vertical

430   layers (~ 2.5 km thick). The v2 forward model reduces the number of half streams from 4 to 2 with a

431   resulting increase in speed of a factor of ~2. To eliminate the increasing RT approximation errors, a

432   look-up table (LUT)-based correction is performed, which enables to adjust the differences in RT

433   variables due to different number of streams (2 vs. 6) and number of layers (24 vs. 72) as well as

434   neglecting polarization effect. As verified in a companion paper, updates improve the retrieval speed by

435   a factor of ~ 3.3 as well as the retrieval accuracy (Bak et al., 2021). Note that the Ring simulation

436   remains unchanged from v1 algorithm; the spectral structure of the Ring signal is externally simulated

437   with the iterative fitting of amplitude of the Ring spectrum and then subtracted from the measured

438   spectral reflectance.

439

440

3.8 Soft calibration

441

442   The left panels of Figure 8 show (a) the spectral fitting residuals averaged in the latitude band of 60ºS
443   to 60ºN, (b) tropospheric column ozone (TCO) distribution, and (c) cross-track dependent stripe errors
444   of TCOs where OMI collection 4 L1b product is applied without any radiometric corrections. As shown,
445   there remain quite persistent residuals of up to ~ 1.0 % in the UV1 range and of up to 0.3 % in the UV2
446   range. The TCO distribution shows the along-track stripes that are commonly found in OMI trace gas
447   products. The cross-track dependent stripes of TCO are evaluated for 18 bands of latitude, as anomalies
448   in the ratio of each cross-track column to the average column taken within cross-track positions 5-25
449   (1-based). The amplitude of anomalies is within ± 10 % at nadir pixels, but reaching to 40 % at off-
450   nadir pixels, with some dependency on latitudes. However, stratospheric column ozone (SCO) retrievals
451   are almost free of stripe errors (not shown here). To reduce the striping, a soft calibration was applied
452   to OMI radiances in OMPROFOZ v1. The soft spectra are derived as a systematic component of
453   differences between measured and simulated radiances at tropical clear-sky pixels in summer where the
454   forward model calculations are more accurate to attribute the residuals to measurement biases. The soft
455   spectra are re-derived for OMI collection 4 L1b product using the v2 forward model calculations (Sect
456   3.7). The ozone profile input is prepared from 10-degree zonal averages of daily MLS measurements
457   above 215 hPa and climatological ozone profiles taken from McPeters and Labow (2012) below. The
458   climatological profile shape is adjusted to account for the daily variability using 10-degree zonal
459   averages of the level 3 OMI TOMS-like total ozone product (OMTO3d). To smooth out the impact of
460   daily ozone variabilities, one-week measurements during July 11-17th over the tropics 20°S-20°N are
461   used in deriving the soft spectra after screening out outliers of extreme viewing geometries (SZA > 60°),
462   cloudy pixels (f_c < 0.2), bright surfaces (A_{sfc} > 0.1), and aerosol contaminated pixels (aerosol index
463   > 5) as well as abnormally large values of average residuals (UV1 > 8, UV2 > 3). Note that the threshold
464   value of filtering out aerosol pixels needs to be relaxed due to the overestimation errors of aerosol index
465   at initial iteration. Figure 9 displays the cross-track dependent soft spectrum for the case of July 2005
466   when instrument degradation is negligible and row-anomaly damage has not occurred. It illustrates the
467   existence of systematic residuals between measured and simulated radiances within 2 % in UV2 and
468   mostly from -7 to 3 % in the UV1, except for some spikes. The right panels of Figure 8 demonstrate
469   how soft calibration works for improving ozone retrievals in comparison to the left panels where soft
470   calibration is tuned off. It is clearly shown that the systematic spikes are mostly eliminated as well as
471   cross-track dependent stipes are globally reduced even up to high-latitudes. In particular, the "anomalies"
472   are reduced to within 0.1 %, except at first cross-track pixels. This calibration has been applied
473   independent of time and latitude in the v1 algorithm. To account for OMI instrument degradation errors,

Atmospheric
Measurement
Techniques
Discussions

Open Access

EGU

474   the v2 soft spectra are developed for every year. As an example, the yearly soft spectra are displayed at

475   several cross-track positions in Figure 10. There is noticeable yearly variation in the UV1 band,

476   typically within 2-3% over 17 years. The most significant degradation features are found at the first

477   cross-track pixel in the UV1 band, with relative change of 5 % or more. For cross-track positions 13,

478   18, 22, correction spectra cannot be derived for most of the time periods after 2008 due to the occurrence

479   of serious row anomaly. Although correction can be derived for cross-track position 13 during 2020, it

480   is significantly different from those before 2008, indicating that it is still affected by row anomaly. The

481   yearly variation in the UV2 band is much smaller, and can be clearly identified below ~315 nm to be

482   within 1 %. However, it could make a significant impact on ozone profile retrievals because the spectral

483   fit residuals need to be smaller than 0.2-0.3 % in the Huggins band for reliable retrieval quality of the

484   tropospheric ozone (Munro et al., 1998).
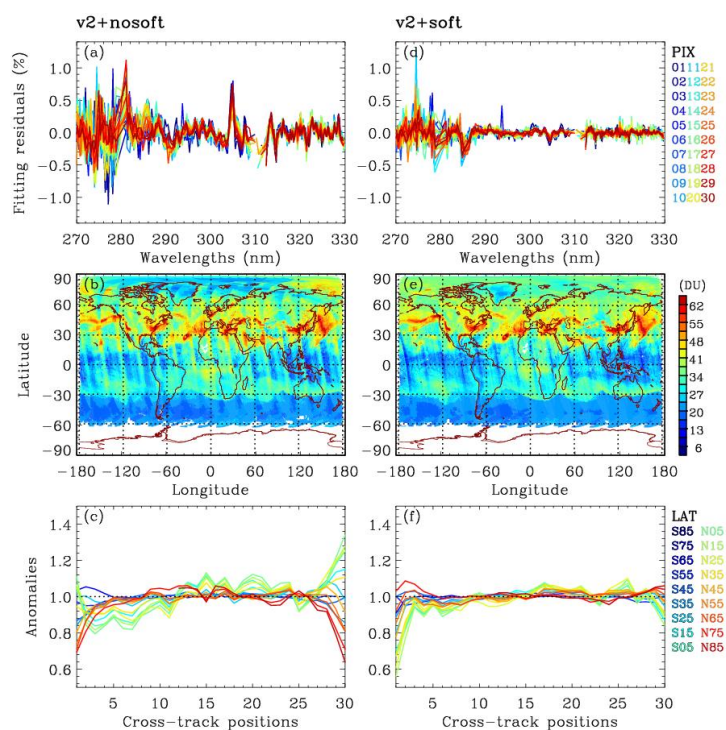
485

486   **Figure 8**. (a, d) Spectral fitting residuals (%) averaged in the latitude of 60°S and 60°N from OMI measurements

487   on 15 June 2006, (b,e) the global distribution of tropospheric column ozone (TCO, DU), and (c,f) anomalies of

488   TCO as a function of 18 latitude bands. Left and right panels are for without and with soft calibration, respectively.
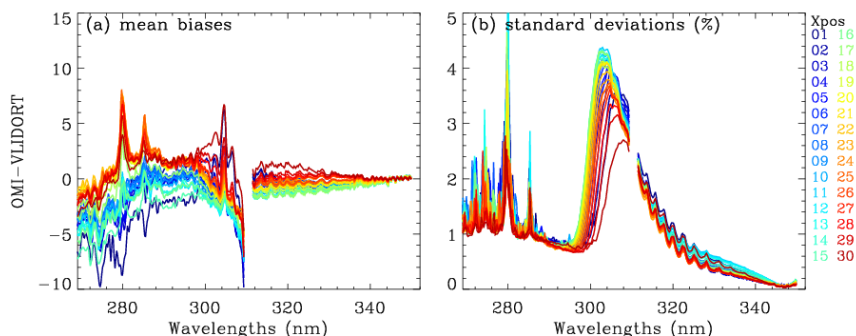
Figure 9 (a) soft calibration spectra derived for collection4 OMI L1b products in July 11-17, 2005, representing the systematic biases between measured and simulated spectrum. (b) the standard deviations of the systematic biases, representing the uncertainties of soft calibration spectra.
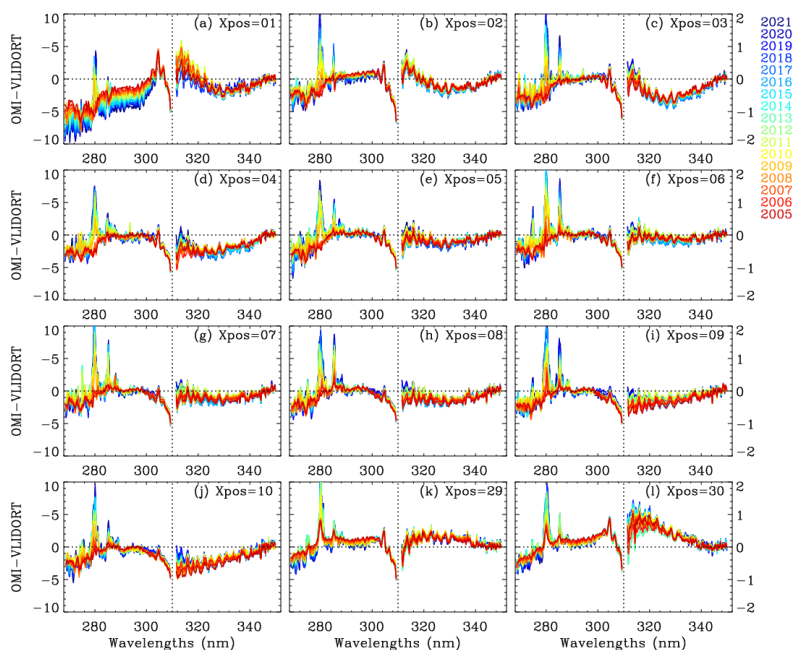

Figure 10. Yearly dependent soft calibration spectra from 2005 to 2021 at several cross-track positions (Xpos, UV1-based) which have been not affected by row anomalies over the mission. Note that the UV1 and UV2 bands are plotted with different Y-axis ranges (left Y-axis for UV1 and right Y-axis for UV2) for better visualization.

3.9 Common mode correction

As compared in Figures 11 left and middle panels, the soft calibration is less effective in eliminating the systematic residuals at high solar zenith angles, especially in the UV2 band where the spectral residuals vary from 0.1 % at lower SZAs to 0.4 % at higher SZAs. This implies the existence of a spectral dependence of the radiometric calibration and detector sensitivity on the signal represented by solar zenith angle, which is not accounted for in the soft calibration dependent only on CCD dimension. Moreover, the soft calibration induces the systematic errors spiking at around ~ 285 nm and 305 nm in the UV1 band. A common mode correction (CMC) is newly implemented in OMPROFOZ v2, to correct the remaining radiometric errors. The common mode spectrum of the fitting residuals is physically treated as a pseudo absorber, along with a scaling coefficient that is iteratively fitted in each of the UV1 and UV2 windows. Therefore, the scene-dependent radiometric errors could be partly accounted for. This kind of correction is originally used in the spectral fitting process where a common mode residual could be calculated on-line for each orbit of measurement. However, additional on-line calculation is not practical for the time-consuming optimal estimation-based ozone profile retrieval process. Therefore, we derive time-independent common mode spectra by averaging three days of fitting residuals (July 13th -15th, 2005) over five solar zenith angle regimes [0°-40°, 40°-60°,60°-70°, 70°-80°, 80°-85°] for each cross-track position. As demonstrated in Figure 11 right panel, the applied common mode spectrum is likely to absorb the remaining spectral errors and hence the fitting accuracy is globally improved. For example, the systematic features are clearly reduced above 285 nm in the UV1 window, but the noisy features are still not well fitted below 285 nm. In the UV2 band, applying CMC reduces the dependence of fitting residuals on both solar zenith angle and cross-track pixels and hence the remaining residuals are globally less than 0.1 % at most wavelengths. As shown in Figures 12, striping patterns of tropospheric ozone retrievals could be reduced due to improvements of retrievals at the first cross-track pixels in the tropics where soft calibration deepens anomalies (Figure 8.f). Comparisons with OMPROFOZ v1 retrievals (Figure 12.d-f) demonstrate that OMPROFOZ v2 product provides global information on tropospheric column ozone with smaller retrievals biases due to radiometric calibration errors and more consistent data quality with respect to different viewing geometries and latitude.

527
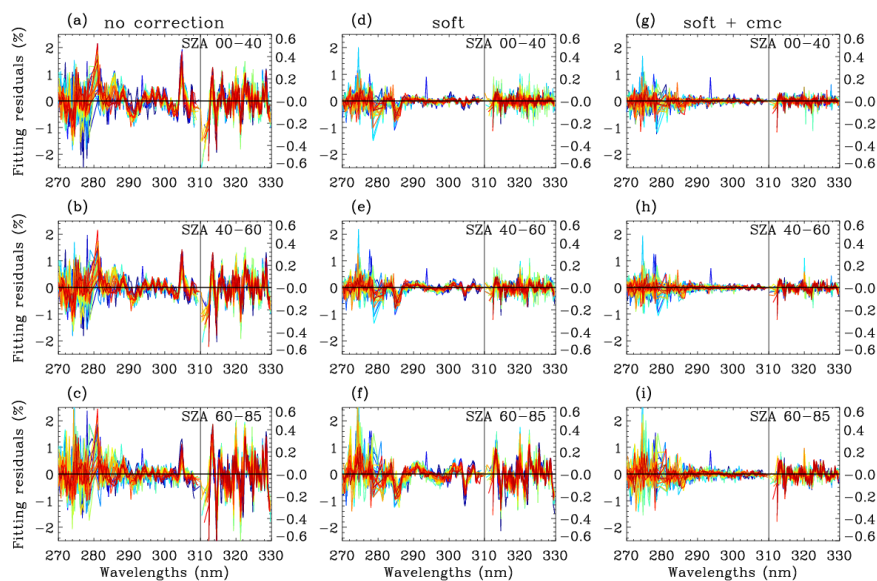
Figure 11. Comparison of spectral fitting residuals (%) averaged for three solar zenith angle regimes (00º-40º, 40º-60º, 60º-85º) from OMI measurements on 15 Jun 2005, with different radiometric calibration settings (left: all radiometric correction is turned off, middle: soft calibration is turned on, right: soft calibration and common model correction are turned on). Note that the residuals are plotted in different y-axis range below (left y-axis) and above (right y-axis) 310 nm, respectively.

533

4. Validation with ozonesonde measurements

535

536   Comparisons against ozonesonde measurements are performed to highlight improvements of data quality and long-term consistency of OMPROFOZ v2 over OMPROFOZ v1. Ozonesonde measurements are obtained from three sites over central Europe during the period of 2005 to 2020, listed in Table 5. Balloon-borne ozone profiles are regularly measured two/three times per week at these sites located close to each other. The coincidence criteria used to pair OMI and ozonesonde measurements are within 100 km and 6 hours and then the closest pair is selected after screening out row anomaly flagged pairs. For comparison, individual ozonesonde soundings are converted from mPa into DU and then interpolated at OMI vertical grids, but without adjusting the vertical resolution into OMI to address the total errors of OMI retrievals including smoothing errors. The relative difference is calculated as (OMI-sonde)/ sonde × 100 %. Extreme values that are beyond the mean by 3σ are dropped in estimating the comparison statistics.
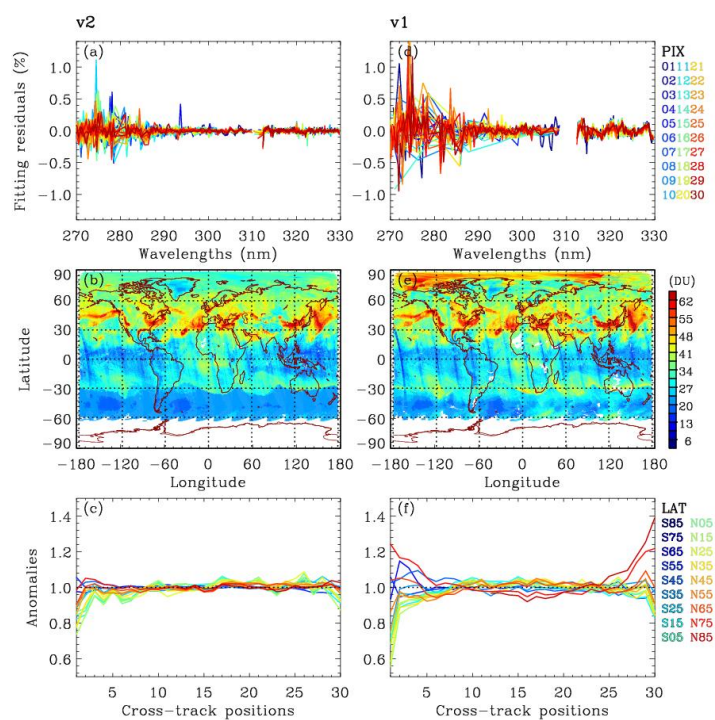
547   Figure 13 shows comparisons of ozone profiles between OMI and ozonesonde during the pre and

548   post Row Anomaly (RA) periods, respectively. The pre-RA period is set to be from the beginning of the

549   mission through 2008 when the row anomalies were relatively not serious and the post-RA period is

550   after that. Both v1 and v2 retrievals are positively biased relative to ozonesonde measurements. The

551   mean biases (MBs) of profile differences are less than 20 % over the layers when OMPROFOZ v2

552   profiles are compared during the pre-RA period. On the other hand, MBs of OMPROFOZ v1 are largely

553   skewed by ~ 45 % in the tropopause region. The comparison also confirms significant improvements

554   of OMPROFOZ v2 retrievals, with the reduction of standard deviations (SDs) by ~ 40 % around the

555   tropopause. These improvements are achieved mainly due to implementing TB ozone profile

556   climatology which could better represent the profile shape in the UTLS as mentioned in Section 3.1.

557   Comparison statistics between OMPROFOZ v2 and ozonesondes profiles are generally consistent

558   before and after the RA occurrence in spite of the inconsistent sampling resulting from the occurrence

559   of RA so that only about half of the OMI measurements remain valid, mostly on the west of nadir during

560   the post-RA period. However, OMPROFOZ v1 profiles are shown to be much more affected by

561   temporal changes of OMI instrumental stability, especially in the lower atmosphere.

562   The rest of this section is concentrated on assessing the consistency of tropospheric ozone retrieval

563   quality with respect to temporal changes. For this comparison, tropospheric ozone columns (TCOs) are

564   integrated over the troposphere between 200 hPa and 900 hPa from ozone profiles to avoid the impact

565   of different meteorological inputs used in V1 and V2 retrievals. In order to check the seasonal changes

566   of retrieval quality, comparison statistics of tropospheric ozone between OMI and ozonesondes are

567   derived for each month during the pre-RA period. The seasonal changes of retrieval quality could be

568   mainly related to the solar zenith angle dependency of OMI measurement sensitivity to the lower

569   tropospheric ozone, which also causes the inconsistency of retrieval quality between lower and higher

570   latitudes. As shown in Figure 14.a, monthly biases of OMI TCO are minimized below ~ 2 DU from

571   June to October when the solar zenith angles are relatively small, commonly for OMPROFOZ v1 and

572   v2. However, the mean biases of OMPROFOZ v1 increase up to ~ 6-9 DU during January-March, while

573   OMPROFOZ v2 show the moderate change of monthly biases from winter to summer, with the smaller

574   SDs of TCO differences by ~3-4 DU during December-March (Fig. 14.b).

575   In order to check the long-term stability, TCO differences are averaged into four seasons for each

576   year from 2005 to 2020 in Figures 14.c and d. The existence of a long-term drift is clear with MBs of

577   OMPROFOZ v1 TCO decreasing from ~ 4.35DU before 2008 to ~ 0.05 DU after 2015. This temporal

578   drift is largely corrected in OMPROFOZ v2 retrievals and the standard deviations of TCO differences

579   are reduced generally over the entire period. In addition, OMPROFOZ v1 shows more spikes in both

580   MBs and SDs than OMPROFOZ v2, especially during the period of 2011 to 2015 when the RA
581   dynamically expands. Those spikes could be attributed to row anomaly-contaminated retrievals
582   unscreened with the KNMI-based row anomaly flags (used in v1) which is considered to be less strict
583   than TOMS-based row anomaly flags (used in v2).

584

585   **Figure 12**. Same as Figure 8, but for V2 (OMI collection 4 product with the final v2 algorithm) and V1 (OMI
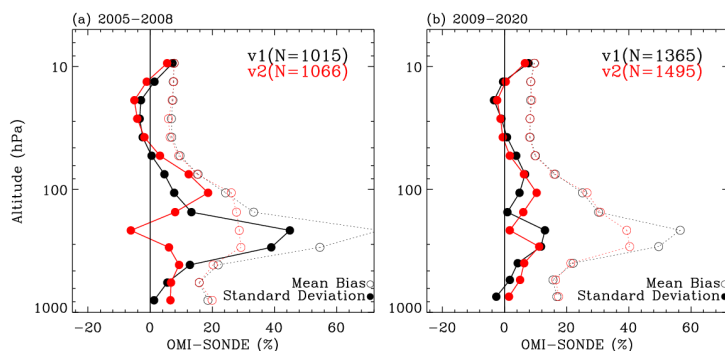586   collection 3 with the v1 algorithm).
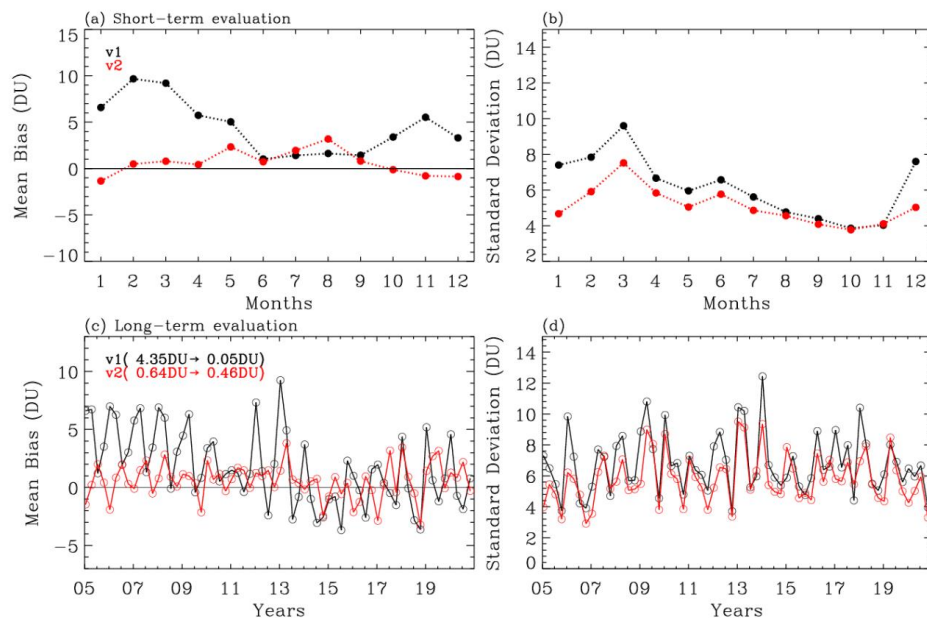
587

588

589

590

591

592

Atmospheric
Measurement
Techniques
Discussions

593

594

Figure 13. Comparisons of ozone profiles between OMI and ozonesonde during (a) pre-row anomaly
and (b) post-row anomaly periods, respectively. OMI retrievals are qualified with RMSE < 3, RMS <
2%, and cloud fraction less than 0.6. The number of coincident pairs (N) is given in legend.

598

599

Figure 14. (a) Monthly mean and (b) corresponding standard deviations in differences of tropospheric column
ozone (TCO, 200-900 hPa) between OMI and ozonesondes during the period of 2005 to 2008. (c,d) is same as
(a,b), but for seasonal differences of TCO from 2005 to 2020. The legend of Fig. c represents the overall mean for
the period of 2005-2008 and 2015-2020, respectively.

604

Atmospheric
Measurement
Techniques
Discussions

Open Access

EGU

5. Summary and Conclusion

The Smithsonian Astrophysical Observatory (SAO) ozone profile retrieval algorithm has been run in NASA's Science Investigator-led Processing System (SIPS) to create the Ozone Monitoring Instrument (OMI) ozone profile (OMPROFOZ) research product. Since the first data release, the efforts to improve the retrieval accuracy and long-term consistency of OMI ozone profile retrievals have continued externally. In this paper, the second version of OMPROFOZ research product is introduced, which will be released at GES-DISC while the first version will continue to be archived at AVDC. One of the major changes is to switch the L1b data from collection 3 to collection 4, for both radiance and irradiance as well as the accompanying auxiliary datasets. We also changed several geophysical and spectroscopic inputs including meteorological data, ozone profile climatology, high-resolution solar reference spectrum, and ozone absorption cross-section dataset. Implementations of forward model calculations and measurements calibrations are improved. The v2 forward model employs a faster principal component analysis (PCA)-based VLIDORT model, along with the LUT-based correction which speeds up the online radiative transfer model calculation while corrections to the approximation produce improved accuracy. The resulting speed-up allows OMI native measurements to be processed for OMPROFOZ v2, with data resolution of 48×26 km^2 at nadir. Note that to meet the computational cost, the previous data were processed after coadding OMI measurements at the spatial resolution of 48×52 km^2. To better represent the shape of OMI slit functions, the slit width and shape factor are parameterized from OMI irradiances, assuming a super Gaussian, instead of a normal Gaussian. Moreover, the effects of slit function differences between radiance and irradiance on ozone retrievals are accounted for as pseudo absorbers in the iterative fit process. The OMI irradiance measurements are included via a monthly average instead of a 3-year climatological mean to cancel out the degradation offset between radiance and irradiance measurements. The empirical soft calibration spectra are re-derived annually to be consistent with the updated implementations to remove the systematic differences between measured and simulated radiances. "Common mode" correction spectra are derived from remaining residual spectra after soft calibration with the dependency on solar zenith angle. The common mode is included as a pseudo absorber in the iterative fit process, which helps to smooth out the discrepancies of ozone retrieval accuracy between lower and higher solar zenith angles and between nadir and off-nadir pixels.

In order to verify improvements of OMPROFOZ data quality, both v1 and v2 ozone profiles are evaluated against ozonesonde measurements taken from central Europe. It is clearly shown that ozone profile retrievals are greatly improved in the troposphere, especially around the tropopause, with the reduction of mean biases by ~ 25 % during the pre-RA season. The standard deviations of mean biases

639   are also improved by ~ 40 % and ~ 20 % before and after the RA occurrence. The comparison with

640   ozonesondes also confirms that the temporal consistency of tropospheric ozone quality is improved.

641   The seasonal change of data quality from summer to winter is predominant in OMI tropospheric ozone

642   with V1 processing. However, OMPROFOZ v2 data quality shows much better consistency, with the

643   seasonal changes of retrieval biases within ~ 2-3 DU. Above all, we validate that the OMI long-term

644   degradation is better accounted for in OMPROROZ v2 processing, along with switching OMI L1b data

645   from collection 3 to collection 4 and updating implementation details. In OMPROFOZ v1, mean biases

646   of tropospheric ozone relative to ozonesonde shows a drift in errors from 4.35 DU to 0.05 DU before

647   and after the RA occurrence, which are greatly reduced to within ± 0.5 DU for both periods in

648   OMPROFOZ v2.

649   This new algorithm has been delivered to the NASA OMI SIPS for operational processing and the

650   reprocessing of the entire mission is in progress. The OMPROFOZ v2 product will be distributed via

651   the NASA GES DISC.

652

653 **Author Contributions** J.B and X.L designed the research. X.L developed the OMPROFOZ v1
654 and J.B updated it to OMPROFOZ v2. K.Y contributed to improving the forward model simulations
655 and transferring codes into SIPS; G.G.A and E.O.S developed the reading modules for OMI collection
656 4 products; K.C advised the update to solar reference spectrum; C.H.K provided financial support to
657 make this study continue. J.B and X.L conducted the research and wrote the paper; all authors
658 contributed to the analysis and writing.

659

660 **Competing interests**. The authors have no competing interests

667

668

669 **Data Availability**
670 All OMI datasets are available at https://disc.gsfc.nasa.gov/ (last access: 15 July 2023). The ozonesonde
671 data used to validate our ozone profile retrievals were obtained though the WOUDC. The WOUDC
672 dataset is available at https://woudc.org/ data/products/ozonesonde/ (last access: 15 July 2023).

673

678

679 **References**

680   AURA-OMI-KNMI-L01B-0005-SD, 2021. Input output data specification for the collection 4 L01b data processing of the
681   Ozone Monitoring Instrument.

682   Bak, J., Baek, K.H., Kim, J.H., Liu, X., Kim, J., Chance, K., 2019a. Cross-evaluation of GEMS tropospheric ozone retrieval
683   performance using OMI data and the use of an ozonesonde dataset over East Asia for validation. Atmos. Meas. Tech.
684   12, 5201–5215. https://doi.org/10.5194/amt-12-5201-2019

685   Bak, J., Coddington, O., Liu, X., Chance, K., Lee, H.J., Jeon, W., Kim, J.H., Kim, C.H., 2022. Impact of using a new high-
686   resolution solar reference spectrum on OMI ozone profile retrievals. Remote Sens. 14, 1–12.
687   https://doi.org/10.3390/rs14010037

688   Bak, J., Liu, X., Birk, M., Wagner, G., Gordon, I.E., Chance, K., 2020. Impact of using a new ultraviolet ozone absorption
689   cross-section dataset on OMI ozone profile retrievals. Atmos. Meas. Tech. 13, 5845–5854.
690   https://doi.org/10.5194/amt-13-5845-2020

691   Bak, J., Liu, X., Kim, J.-H., Haffner, D.P., Chance, K., Yang, K., Sun, K., 2017. Characterization and correction of OMPS
692   nadir mapper measurements for ozone profile retrievals. Atmos. Meas. Tech. 10, 4373–4388.
693   https://doi.org/10.5194/amt-10-4373-2017

694   Bak, J., Liu, X., Spurr, R., Yang, K., Nowlan, C.R., Miller, C.C., Abad, G.G., Chance, K., 2021. Radiative transfer
695   acceleration based on the principal component analysis and lookup table of corrections: optimization and application
696   to UV ozone profile retrievals. Atmos. Meas. Tech. 14, 2659–2672. https://doi.org/10.5194/amt-14-2659-2021

697   Bak, J., Liu, X., Sun, K., Chance, K., Kim, J.-H., 2019b. Linearization of the effect of slit function changes for improving
698   Ozone Monitoring Instrument ozone profile retrievals. Atmos. Meas. Tech. 12, 3777–3788.
699   https://doi.org/10.5194/amt-12-3777-2019

700   Bak, J., Liu, X., Wei, J.C., Pan, L.L., Chance, K., Kim, J.H., 2013. Improvement of omi ozone profile retrievals in the upper
701   troposphere and lower stratosphere by the use of a tropopause-based ozone profile climatology. Atmos. Meas. Tech.
702   6, 2239–2254. https://doi.org/10.5194/amt-6-2239-2013

703   Cai, Z., Liu, Y., Liu, X., Chance, K., Nowlan, C.R., Lang, R., Munro, R., Suleiman, R., 2012. Characterization and
704   correction of global ozone monitoring experiment 2 ultraviolet measurements and application to ozone profile
705   retrievals. J. Geophys. Res. Atmos. 117, 1–16. https://doi.org/10.1029/2011JD017096

706   Chance, K., Kurucz, R.L., 2010. An improved high-resolution solar reference spectrum for earth's atmosphere
707   measurements in the ultraviolet, visible, and near infrared. J. Quant. Spectrosc. Radiat. Transf. 111, 1289–1295.
708   https://doi.org/10.1016/j.jqsrt.2010.01.036

709   Coddington, O.M., Richard, E.C., Harber, D., Pilewskie, P., Woods, T.N., Chance, K., Liu, X., Sun, K., 2021. The TSIS-1
710   Hybrid Solar Reference Spectrum. Geophys. Res. Lett. 1–10. https://doi.org/10.1029/2020gl091709

711   Gaudel, A., Cooper, O.R., Ancellet, G., Barret, B., Boynard, A., Burrows, J.P., Clerbaux, C., Coheur, P.-F., Cuesta, J.,
712   Cuevas, E., Doniki, S., Dufour, G., Ebojie, F., Foret, G., Garcia, O., Granados-Muñoz, M.J., Hannigan, J.W., Hase, F.,
713   Hassler, B., Huang, G., Hurtmans, D., Jaffe, D., Jones, N., Kalabokas, P., Kerridge, B., Kulawik, S., Latter, B.,
714   Leblanc, T., Le Flochmoën, E., Lin, W., Liu, J., Liu, X., Mahieu, E., McClure-Begley, A., Neu, J.L., Osman, M.,
715   Palm, M., Petetin, H., Petropavlovskikh, I., Querel, R., Rahpoe, N., Rozanov, A., Schultz, M.G., Schwab, J., Siddans,
716   R., Smale, D., Steinbacher, M., Tanimoto, H., Tarasick, D.W., Thouret, V., Thompson, A.M., Trickl, T.,
717   Weatherhead, E., Wespes, C., Worden, H.M., Vigouroux, C., Xu, X., Zeng, G., Ziemke, J., 2018. Tropospheric Ozone
718   Assessment Report: Present-day distribution and trends of tropospheric ozone relevant to climate and global
719   atmospheric chemistry model evaluation. Elem. Sci. Anthr. 6, 39. https://doi.org/10.1525/elementa.291

720   Hayashida, S., Liu, X., Ono, A., Yang, K., Chance, K., 2015. Observation of ozone enhancement in the lower troposphere
721   over East Asia from a space-borne ultraviolet spectrometer. Atmos. Chem. Phys. 15, 9865–9881.
722   https://doi.org/10.5194/acp-15-9865-2015

723   Hu, L., Jacob, D.J., Liu, X., Zhang, Y., Zhang, L., Kim, P.S., Sulprizio, M.P., Yantosca, R.M., 2017. Global budget of
724   tropospheric ozone: Evaluating recent model advances with satellite (OMI), aircraft (IAGOS), and ozonesonde
725   observations. Atmos. Environ. 167, 323–334. https://doi.org/10.1016/j.atmosenv.2017.08.036

726   Huang, G., Liu, X., Chance, K., Yang, K., Bhartia, P.K., Cai, Z., Allaart, M., Ancellet, G., Calpini, B., Coetzee, G.J.R.,
727   Cuevas-Agulló, E., Cupeiro, M., De Backer, H., Dubey, M.K., Fuelberg, H.E., Fujiwara, M., Godin-Beekmann, S.,
728   Hall, T.J., Johnson, B., Joseph, E., Kivi, R., Kois, B., Komala, N., König-Langlo, G., Laneve, G., Leblanc, T.,
729   Marchand, M., Minschwaner, K.R., Morris, G., Newchurch, M.J., Ogino, S.-Y., Ohkawara, N., Piters, A.J.M., Posny,
730   F., Querel, R., Scheele, R., Schmidlin, F.J., Schnell, R.C., Schrems, O., Selkirk, H., Shiotani, M., Skriváncková, P.,
731   Stübi, R., Taha, G., Tarasick, D.W., Thompson, A.M., Thouret, V., Tully, M.B., Van Malderen, R., Vömel, H., von

Atmospheric
Measurement
Techniques
Discussions

732   der Gathen, P., Witte, J.C., Yela, M., 2017. Validation of 10-year SAO OMI Ozone Profile (PROFOZ) product using
733   ozonesonde observations. Atmos. Meas. Tech. 10, 2455–2475. https://doi.org/10.5194/amt-10-2455-2017

734   Huang, G., Liu, X., Chance, K., Yang, K., Cai, Z., 2018. Validation of 10-year SAO OMI ozone profile (PROFOZ) product
735   using Aura MLS measurements. Atmos. Meas. Tech. 11, 17–32. https://doi.org/10.5194/amt-11-17-2018

736   Kleipool, Q., Rozemeijer, N., van Hoek, M., Leloux, J., Loots, E., Ludewig, A., van der Plas, E., Adrichem, D., Harel, R.,
737   Spronk, S., ter Linden, M., Jaross, G., Haffner, D., Veefkind, P., Levelt, P.F., 2022. Ozone Monitoring Instrument
738   (OMI) collection 4: establishing a 17-year-long series of detrended level-1b data. Atmos. Meas. Tech. 15, 3527–3553.
739   https://doi.org/10.5194/amt-15-3527-2022

740   Kuang, S., Newchurch, M.J., Johnson, M.S., Wang, L., Burris, J., Pierce, R.B., Eloranta, E.W., Pollack, I.B., Graus, M., de
741   Gouw, J., Warneke, C., Ryerson, T.B., Markovic, M.Z., Holloway, J.S., Pour-Biazar, A., Huang, G., Liu, X., Feng,
742   N., 2017. Summertime tropospheric ozone enhancement associated with a cold front passage due to stratosphere-to-
743   troposphere transport and biomass burning: Simultaneous ground-based lidar and airborne measurements. J. Geophys.
744   Res. Atmos. 122, 1293–1311. https://doi.org/https://doi.org/10.1002/2016JD026078

745   Liu, C., Liu, X., Chance, K., 2013. The impact of using different ozone cross sections on ozone profile retrievals from OMI
746   UV measurements. J. Quant. Spectrosc. Radiat. Transf. 130, 365–372. https://doi.org/10.1016/j.jqsrt.2013.06.006

747   Liu, X., Bhartia, P.K., Chance, K., Spurr, R.J.D., Kurosu, T.P., 2010. Ozone profile retrievals from the Ozone Monitoring
748   Instrument. Atmos. Chem. Phys. 10, 2521–2537. https://doi.org/10.5194/acp-10-2521-2010

749   Liu, X., Chance, K., Sioris, C.E., Kurosu, T.P., 2007. Impact of using different ozone cross sections on ozone profile
750   retrievals from Global Ozone Monitoring Experiment (GOME) ultraviolet measurements. Atmos. Chem. Phys. 7,
751   3571–3578. https://doi.org/10.5194/acp-7-3571-2007

752   Liu, X., Chance, K., Sioris, C.E., Spurr, R.J.D., Kurosu, T.P., Martin, R. V., Newchurch, M.J., 2005. Ozone profile and
753   tropospheric ozone retrievals from the Global Ozone Monitoring Experiment: Algorithm description and validation. J.
754   Geophys. Res. 110, D20307. https://doi.org/10.1029/2005JD006240

755   Lu, X., Zhang, L., Liu, X., Gao, M., Zhao, Y., Shao, J., 2018. Lower tropospheric ozone over India and its linkage to the
756   South Asian monsoon. Atmos. Chem. Phys. 18, 3101–3118. https://doi.org/10.5194/acp-18-3101-2018

757   Luo, J., Pan, L.L., Honomichl, S.B., Bergman, J.W., Randel, W.J., Francis, G., Clerbaux, C., George, M., Liu, X., Tian, W.,
758   2018. Space-time variability in UTLS chemical distribution in the Asian summer monsoon viewed by limb and nadir
759   satellite sensors. Atmos. Chem. Phys. 18, 12511–12530. https://doi.org/10.5194/acp-18-12511-2018

760   McPeters, R.D., Labow, G.J., 2012. Climatology 2011: An MLS and sonde derived ozone climatology for satellite retrieval
761   algorithms. J. Geophys. Res. Atmos. 117. https://doi.org/https://doi.org/10.1029/2011JD017006

762   McPeters, R.D., Labow, G.J., Logan, J.A., 2007. Ozone climatological profiles for satellite retrieval algorithms. J. Geophys.
763   Res. 112, D05308. https://doi.org/10.1029/2005JD006823

764   Munro, R., Siddans, R., Reburn, W.J., Kerridge, B.J., 1998. Direct measurement of tropospheric ozone distributions from
765   space. Nature 392, 168–171. https://doi.org/10.1038/32392

766   Orphal, J., Staehelin, J., Tamminen, J., Braathen, G., De Backer, M.-R., Bais, A., Balis, D., Barbe, A., Bhartia, P.K., Birk,
767   M., Burkholder, J.B., Chance, K., von Clarmann, T., Cox, A., Degenstein, D., Evans, R., Flaud, J.-M., Flittner, D.,
768   Godin-Beekmann, S., Gorshelev, V., Gratien, A., Hare, E., Janssen, C., Kyrölä, E., McElroy, T., McPeters, R., Pastel,
769   M., Petersen, M., Petropavlovskikh, I., Picquet-Varrault, B., Pitts, M., Labow, G., Rotger-Languereau, M., Leblanc,
770   T., Lerot, C., Liu, X., Moussay, P., Redondas, A., Van Roozendael, M., Sander, S.P., Schneider, M., Serdyuchenko,
771   A., Veefkind, P., Viallon, J., Viatte, C., Wagner, G., Weber, M., Wielgosz, R.I., Zehner, C., 2016. Absorption cross-
772   sections of ozone in the ultraviolet and visible spectral regions: Status report 2015. J. Mol. Spectrosc. 327, 105–121.
773   https://doi.org/https://doi.org/10.1016/j.jms.2016.07.007

774   Schenkeveld, V.M.E., Jaross, G., Marchenko, S., Haffner, D., Kleipool, Q.L., Rozemeijer, N.C., Veefkind, J.P., Levelt, P.F.,
775   2017. In-flight performance of the Ozone Monitoring Instrument. Atmos. Meas. Tech. 10, 1957–1986.
776   https://doi.org/10.5194/amt-10-1957-2017

777   Sun, K., Liu, X., Huang, G., González Abad, G., Cai, Z., Chance, K., Yang, K., 2017. Deriving the slit functions from OMI
778   solar observations and its implications for ozone-profile retrieval. Atmos. Meas. Tech. 10, 3677–3695.
779   https://doi.org/10.5194/amt-10-3677-2017

780   Walker, T.W., Martin, R. V., Van Donkelaar, A., Leaitch, W.R., MacDonald, A.M., Anlauf, K.G., Cohen, R.C., Bertram,
781   T.H., Huey, L.G., Avery, M.A., Weinheimer, A.J., Flocke, F.M., Tarasick, D.W., Thompson, A.M., Streets, D.G., Liu,

782   X., 2010. Trans-pacific transport of reactive nitrogen and ozone to Canada during spring. Atmos. Chem. Phys. 10,
783   8353–8372. https://doi.org/10.5194/acp-10-8353-2010

784   Wei, J., Li, Z., Li, K., Dickerson, R.R., Pinker, R.T., Wang, J., Liu, X., Sun, L., Xue, W., Cribb, M., 2022. Full-coverage
785   mapping and spatiotemporal variations of ground-level ozone (O3) pollution from 2013 to 2020 across China. Remote
786   Sens. Environ. 270. https://doi.org/10.1016/j.rse.2021.112775

787   Zhang, L., Jacob, D.J., Liu, X., Logan, J.A., Chance, K., Eldering, A., Bojkov, B.R., 2010. Intercomparison methods for
788   satellite measurements of atmospheric composition: Application to tropospheric ozone from TES and OMI. Atmos.
789   Chem. Phys. 10, 4725–4739. https://doi.org/10.5194/acp-10-4725-2010

790   Zhao, F., Liu, C., Cai, Z., Liu, X., Bak, J., Kim, J., Hu, Q., Xia, C., Zhang, C., Sun, Y., Wang, W., Liu, J., 2021. Ozone
791   profile retrievals from TROPOMI: Implication for the variation of tropospheric ozone during the outbreak of COVID-
792   19 in China. Sci. Total Environ. 764, 142886. https://doi.org/10.1016/j.scitotenv.2020.142886

793   Ziemke, J.R., Olsen, M.A., Witte, J.C., Douglass, A.R., Strahan, S.E., Wargan, K., Liu, X., Schoeberl, M.R., Yang, K.,
794   Kaplan, T.B., Pawson, S., Duncan, B.N., Newman, P.A., Bhartia, P.K., Heney, M.K., 2014. Assessment and
795   applications of NASA ozone data products derived from Aura OMI/MLS satellite measurements in context of the
796   GMI chemical transport model. J. Geophys. Res. Atmos. 119, 5671–5699.
797   https://doi.org/https://doi.org/10.1002/2013JD020914

798   Zoogman, P., Liu, X., Suleiman, R.M., Pennington, W.F., Flittner, D.E., Al-Saadi, J.A., Hilton, B.B., Nicks, D.K.,
799   Newchurch, M.J., Carr, J.L., Janz, S.J., Andraschko, M.R., Arola, A., Baker, B.D., Canova, B.P., Chan Miller, C.,
800   Cohen, R.C., Davis, J.E., Dussault, M.E., Edwards, D.P., Fishman, J., Ghulam, A., González Abad, G., Grutter, M.,
801   Herman, J.R., Houck, J., Jacob, D.J., Joiner, J., Kerridge, B.J., Kim, J., Krotkov, N.A., Lamsal, L., Li, C., Lindfors,
802   A., Martin, R. V., McElroy, C.T., McLinden, C., Natraj, V., Neil, D.O., Nowlan, C.R., O'Sullivan, E.J., Palmer, P.I.,
803   Pierce, R.B., Pippin, M.R., Saiz-Lopez, A., Spurr, R.J.D., Szykman, J.J., Torres, O., Veefkind, J.P., Veihelmann, B.,
804   Wang, H., Wang, J., Chance, K., 2017. Tropospheric emissions: Monitoring of pollution (TEMPO). J. Quant.
805   Spectrosc. Radiat. Transf. 186, 17–39. https://doi.org/10.1016/j.jqsrt.2016.05.008

806   <references for OMI products>

807   Kleipool, Q. (2021a), OMI/Aura Level 1B Averaged Solar Irradiances V004, Greenbelt, MD, USA, Goddard Earth Sciences
808   Data and Information Services Center (GES DISC), Accessed: [2023-07-21], 10.5067/Aura/OMI/DATA1401, 2021a

809   Kleipool, Q. (2021b), OMI/Aura Level 1B UV Global Geolocated Earthshine Radiances V004, Greenbelt, MD, USA, Goddard
810   Earth   Sciences   Data   and   Information   Services   Center   (GES   DISC),   Accessed: [2023-07-
811   21],10.5067/AURA/OMI/DATA1402

812   Joiner, J. (2023,a), GEOS-5 FP-IT 3D Time-Averaged Single-Level Diagnostics Geo-Colocated to OMI/Aura UV2 1-Orbit
813   L2 Swath 13x24km V4, NASA Goddard Space Flight Center, Goddard Earth Sciences Data and Information Services
814   Center (GES DISC), Accessed: [2023-07-21], 10.5067/Aura/OMI/DATA2435

815   Joiner, J. (2023,b), GEOS-5 FP-IT 3D Time-Averaged Model-Layer Assimilated Data Geo-Colocated to OMI/Aura VIS 1-
816   Orbit L2 Swath 13x24km V4, NASA Goddard Space Flight Center, Goddard Earth Sciences Data and Information
817   Services Center (GES DISC), Accessed: [2023-07-21], 10.5067/Aura/OMI/DATA2436

818   Joiner, J. (2023,c), Primary Ancillary Data Geo-Colocated to OMI/Aura UV2 1-Orbit L2 Swath 13x24km V4, NASA Goddard
819   Space Flight Center, Goddard Earth Sciences Data and Information Services Center (GES DISC), Accessed: [2023-07-
820   21], 10.5067/Aura/OMI/DATA2438

821   Veefkind, P (2012), OMI/Aura Cloud Pressure and Fraction (O2-O2 Absorption) Daily L2 Global Gridded 0.25 degree x 0.25
822   degree V3, Greenbelt, MD, USA, Goddard Earth Sciences Data and Information Services Center (GES DISC),
823   Accessed: [2023-07-21], 10.5067/Aura/OMI/DATA2008

824   Kleipool, Q (2010), OMI/Aura Surface Reflectance Climatology L3 Global Gridded 0.5 degree x 0.5 degree V3, Greenbelt,
825   MD, USA, Goddard Earth Sciences Data and Information Services Center (GES DISC), Accessed: [2023-07-
826   21], 10.5067/Aura/OMI/DATA3006

827   Bhartia, P.K (2012), OMI/Aura TOMS-Like Ozone, Aerosol Index, Cloud Radiance Fraction L3 1 day 1 degree x 1 degree
828   V3, NASA Goddard Space Flight Center, Goddard Earth Sciences Data and Information Services Center (GES DISC),
829   Accessed: [2023-07-21], 10.5067/Aura/OMI/DATA3001